The Cryosphere Discuss., 8, 4397–4430, 2014
www.the-cryosphere-discuss.net/8/4397/2014/
doi:10.5194/tcd-8-4397-2014

The Cryosphere Discussions
Open Access

Seismic wave propagation in anisotropic ice – Part 2: Effects of crystal anisotropy in geophysical data

A. Diez[1,2], O. Eisen[1], C. Hofstede[1], A. Lambrecht[3], C. Mayer[3], H. Miller[1], D. Steinhage[1], T. Binder[4,*], and I. Weikusat[1,5]

[1]Alfred Wegener Institute Helmholtz Centre for Polar and Marine Research, Bremerhaven, Germany
[2]Karlsruhe Institute of Technology, Karlsruhe, Germany
[3]Bavarian Academy for Sciences and Humanities, Munich, Germany
[4]Interdisciplinary Center for Scientific Computing, University of Heidelberg, Heidelberg, Germany
[5]Department of Geosciences, Eberhard Karls University of Tübingen, Tübingen, Germany
[*]now at: Alfred Wegener Institute Helmholtz Centre for Polar and Marine Research, Bremerhaven, Germany

Received: 18 June 2014 – Accepted: 9 July 2014 – Published: 4 August 2014

Correspondence to: A. Diez (anja.diez@awi.de)

Published by Copernicus Publications on behalf of the European Geosciences Union.

Abstract

We investigate the propagation of seismic waves in anisotropic ice. Two effects are important: (i) sudden changes in crystal orientation fabric (COF) lead to englacial reflections; (ii) the anisotropic fabric induces an angle dependency on the seismic velocities and, thus, recorded traveltimes. Velocities calculated from the polycrystal elasticity tensor derived for the anisotropic fabric from measured COF eigenvalues of the EDML ice core, Antarctica, show good agreement with the velocity trend determined from a vertical seismic profiling. The agreement of the absolute velocity values, however, depends on the choice of the monocrystal elasticity tensor used for the calculation of the polycrystal properties. With this validation of seismic velocities we make use of abrupt changes in COF as common reflection mechanism for seismic and radar data below the firn–ice transition to investigate their occurrence by comparison with ice-core data. Our results highlight the possibility to complement regional radar surveys with local, surface-based seismic deployment to separate isochrones in radar data from other mechanisms. This is important for the reconnaissance of future ice-core drill sites, where accurate isochrone (i.e. non-COF) layer integrity allows for synchronization with other cores, as well as studies of ice dynamics considering non-homogeneous viscosity from preferred crystal orientations.

1 Introduction

To understand the behaviour of glaciers and ice sheets we need measurements to determine the conditions of glaciers at the surface, at the base and within the ice mass. In-situ measurement of englacial physical properties can only be gained by drilling of boreholes and analysis of ice cores. From an ice core information in high vertical resolution can be gained at one specific location on properties like density, conductivity or the size and orientation of ice crystals (Cuffey and Paterson, 2010). To be able to collect information about the spatial distribution of these physical properties beyond the

TCD
8, 4397–4430, 2014

~ 10 cm resolution of ice cores we use surface based radar and seismic measurements to determine englacial conditions.

The propagation of radar waves is mainly influenced by density, conductivity, crystal orientation fabric (COF) and temperature. The propagation of seismic waves is mainly influenced by density, COF and temperature. The influence of the temperature on the wave velocity is rather small in both cases (e.g. Matsuoka et al., 1997; Gammon et al., 1983). Below the firn–ice transition the common mechanism influencing the propagation of seismic and radar waves is a preferred orientation of the anisotropic, hexagonal ice crystals. This fabric anisotropy is normally described in form of the COF eigenvalues obtained from ice-core measurements. For both wave types a preferred orientation of the ice crystals has an influence on the wave propagation speed. In addition, an abrupt change in COF causes partial reflections of propagating wave energy.

A linear relationship exists to calculate the relative dielectric permittivity from the measured eigenvalues (Fujita et al., 2000). Hence, the velocity of the radar wave in anisotropic ice as well as the reflection coefficient can be approximately calculated. In order to calculate seismic velocities and reflection coefficients for different anisotropic ice fabrics we presented a framework to derive the anisotropic polycrystal elasticity tensor from COF eigenvalues in Part 1 of this work (Diez et al., 2014). We apply this here to calculate seismic velocities from COF eigenvalues measured along the EDML ice core, retrieved at Kohnen station, Dronning Maud Land, Antarctica (EDML: EPICA Dronning Maud Land, EPICA: European Project for Ice Coring in Antarctica).

In Sect. 2 we introduce the field site and data sets, followed by a short summary on the calculation of the polycrystal elasticity tensor from COF eigenvalues (Part 1, Diez et al., 2014) in Sect. 3. We present results of a vertical seismic profiling (VSP) measurement carried out within the EDML borehole in Sect. 4 and compare the velocity profile derived from the traveltimes of the direct waves to the velocities we derive from the COF eigenvalues of the EDML ice core. Both velocity profiles show the same velocity trend. However, the absolute velocity values of the COF-based profile depend on the choice of the monocrystal elasticity tensor measured by different authors.

TCD
8, 4397–4430, 2014

The last part (Sect. 5) then focuses on the influence of the anisotropic fabric on the observed reflection signature of seismic and radar waves. We investigate the reflection signals visible in the seismic and radar data from Kohnen station and compare them to the measured COF eigenvalues to determine COF-induced reflections. This allows us to identify purely conductivity-induced reflections in the radar data, which are layers of equal age and can, thus, be used safely to laterally extrapolate the age of the ice along the reflections.

2 Field data at Kohnen station

Kohnen station (75.002° S, 0.067° E, WGS84) is located on the Antarctic plateau at an elevation of about 2900 m a.s.l. and some 550 km South-East of the German overwintering station Neumayer III (Fig. 1). Within the EPICA Project an ice core (EDML) has been drilled during 2001 and 2006, down to a depth of 2774 m (Oerter et al., 2009). The overall thickness of the ice was estimated from radar data to 2782 ± 10 m (Oerter et al., 2009).

2.1 Ice core and radar data

Measurements of the density and dielectric properties were carried out along the EDML ice core by means of γ-attenuation profiling (GAP) and dielectrical profiling (DEP), down to a depth of 448 m and 2565 m, respectively (Eisen et al., 2006). After first complete temperature logging in 2005 (Wilhelms et al., 2007) a re-measurement was done in January 2011. The temperature range of −44 °C to −7 °C was determined in the undisturbed borehole between 80.05–2591.44 m depth. Grain radius was also re-measured along the ice core in ∼ 10 m intervals (Binder, 2014) with higher resolution than in previous measurements (Weikusat et al., 2009).

COF measurements (Fig. 2a) were carried out along the EDML ice core between 104–2563 m depth (Hamann et al., 2005; Eisen et al., 2007). After the ice core

TCD
8, 4397–4430, 2014

was stored at −30 °C the c-axes distribution was determined in 2005 on horizontal (0.5 mm × 50 mm × 50 mm) and vertical (0.5 mm × 50 mm × 100 mm) thin sections, in ∼ 50 m intervals, using an automatic fabric analyser. The derived eigenvalues from the horizontal and vertical sections show some variations within ±0.1 which are attributed to the cutting of the samples and, thus, exclusion of certain grains (Eisen et al., 2007; Drews et al., 2013). Statistical weighting was done per grain for the calculation of the COF eigenvalues. The results show cone fabrics in the upper and lower part of the ice sheet and different girdle distributions within.

Radar data sets from the region (Fig. 1) include profiles with 60 ns and 600 ns pulse (Profile 022150) recorded during flight with the AWI research aircraft Polar 2. Additionally, a survey was carried out with the aircraft sliding on the ground in a circle with a radius of about 50 m and 6 legs crossing the circle in different directions using a 60 ns pulse (Profile 033042, Fig. 1, inset).

The radar measurements, in combination with the COF measurements, were used in a study by Eisen et al. (2007) to reveal a strong radar reflector at 2035 m depth caused by a transition of girdle fabric distribution to a narrow cone fabric distribution. Drews et al. (2013) attributed a change in the azimuthal radar backscatter over depth to a change in COF. Both, Eisen et al. (2007) and Drews et al. (2013), concluded from the observed reflection pattern an orientation of the girdle fabric parallel to the ice divide.

2.2 Seismic measurements

Seismic measurements close to the drill site of the EDML ice core were carried out in January 2012 and 2013. The measurements included wideangle and a VSP surveys. For data recording three-component (3C) geophones as well as a streamer and a borehole geophone were used. We carried out explosive and vibroseis surveys using boosters as well as denotation cord for the explosive surveys. Vibroseis surveys employed the micro-vibrator ElViS and the 12 t-vibrator system EnviroVibe (IVI, USA) with a peak force of 66 kN (Eisen et al., 2014).

TCD
8, 4397–4430, 2014

For the VSP measurement a borehole geophone was lowered to a depth of 2580 m in the borehole. Shooting the VSP data set was done in two steps. First, 10 m detonation cord (10 g m^{-1} Pentolite, survey 20120545) was used as coiled-up source, always at the same location on the surface. The borehole geophone was pulled upwards from 2580 m to 100 m depth in 40 m intervals. A day later the same measurement was carried out with boosters (150 g Pentolite, survey 20120546) as source on the same location as the detonation cord, but in a depth interval between 2560 m and 1600 m, again in 40 m steps. By combining both measurements the depth intervals below 1600 m were effectively reduced to 20 m intervals. The depth provided here is given with respect to the top of the borehole casing, which was 13.5 m below the January 2012 surface. The shot location at the surface was 30 m away from the borehole towards the South-Southeast (Fig. 3). For data recording Geodes (Geometrics Inc., USA) were used, with a sample interval of 0.25 ms and a record length of 5 s. During VSP recording the generator of the close-by Kohnen station was always disconnected from the Kohnen power supply grid to avoid strong, 50 Hz generator-produced noise.

Simultaneously to the operation of the borehole geophone a line of 24 3C-geophones was placed about 100 m south of the shot. Borehole and 3C-geophone data were recorded with a sample interval of 0.25 ms and a record length of 5 s on the same Geodes. The 3C data were used to evaluate the reproducibility of different shots and compare the quality of the detonation cord and booster survey.

Next to the VSP measurement wideangle surveys were carried out (Fig. 1) parallel (survey 20120531) and perpendicular (survey 20120532/20120537) to the ice divide, with explosive as well as vibroseis sources. For the recording we used a 60 channel snow streamer with a total spread of 1475 m and 25 m channel spacing. Each channel consists of 8 geophones. For the recording of the different surveys Geodes as well as the StrataView acquisition systems were used.

The wideangle data sets were processed with the focus on analysing englacial reflectors. As it was not possible to clearly identify englacial signals within the shot gathers after processing, we used the velocities determined during the VSP survey to carry out

TCD
8, 4397–4430, 2014

a normal-moveout correction. We stacked 60 traces of each available shot, assuming that englacial layer boundaries are surface parallel and laterally homogeneous. This significantly improved the signal-to-noise ratio, allowing the identification of englacial reflection events. The clearest signals could be observed in data from an explosive shot (5.6 kg Pentolite) that was carried out in a 30 m deep borehole (20120537). This shot shows the highest frequency content and the least amount of disturbing surface waves. We will use this stacked trace for comparison of seismic, radar and ice-core data in Sect. 5.

3 Calculation of seismic velocities for anisotropic ice

We briefly summarize our approach introduced in Part 1 of this work (Diez et al., 2014) to calculate seismic velocities from the COF eigenvalues. In a first step we distinguish between different fabrics based on the COF eigenvalues and calculate two opening angles φ and χ. The opening angles give the extent of the enveloping of the c-axes distribution. One of the opening angles is already determined by the fabric classification, for which we distinguish between cone fabrics ($\varphi = \chi$), thick girdle ($\varphi = 90^\circ$, χ) and partial girdle fabrics ($\chi = 0^\circ$, φ). The elasticity tensor of the polycrystal is then calculated by integrating a measured elasticity tensor with a normal density distribution using these opening angles (Part 1, Diez et al., 2014).

Elasticity tensors of ice were measured by different authors, by means of a range of methods including Brillouin-spectroscopy, ultrasonic sounding, the Schaefer–Bergman method or the analysis of resonance frequencies. These different elasticity tensors are listed in Table 1. These measured elasticity tensors are used to calculate the anisotropic polycrystal elasticity tensor for the different fabrics and from these seismic velocities. Different exact and approximate solutions exist for the calculation of phase and group velocities for different anisotropic fabrics. Here, we use the equations derived by Daley and Krebes (2004) for the calculation of phase velocities for orthorhombic media (Part 1, Diez et al., 2014).

TCD
8, 4397–4430, 2014

Applying this approach to the COF eigenvalue data of the EDML ice core (Fig. 2a) we find the following classifications for the c-axis fabrics (Fig. 2b). Down to a depth of 450 m a cone fabric with large opening angles ($\varphi = \chi \geq 70^{\circ}$) is derived from the eigenvalues, i.e. a fabric close to isotropic. At this depth the eigenvalues show a distinct jump to a more anisotropic fabric. Here, we obtain a cone fabric with opening angles between 55° and 80°. At the depth of 800 m a change to a thick girdle fabric follows. The eigenvalues show larger variations in the eigenvalues λ_2 and λ_3 from this depth downward. Nevertheless, this change in the eigenvalues of λ_2 and λ_3 is a gradual change, not a distinct jump in the available resolution of COF data. Below 1150 m depth a partial girdle fabric can be observed with decreasing opening angle φ with depth and the onset of a cone fabric with opening angles around 35° at 1800 m depth, interrupted by thin regions of partial girdle fabric. A strong cone fabric with opening angles between 10° and 33° is observed below 2040 m, interrupted by a thin (~ 30 m) layer of girdle fabric.

Figure 2c shows as an example the zero-offset logitudinal pressure (P)-wave velocity v_{p0} calculated from the monocrystal elasticity tensor measured by Gammon et al. (1983) converted to the polycrystal elasticity tensor and seismic velocities with our method mentioned above. In the following and if not stated differently we will always use the elasticity tensor measured by Gammon et al. (1983) for our calculation. In the upper 450 m we determine velocities of about 3870 m s^{-1} with only little variations, followed by slightly higher velocities and a change to lower velocities again at 850 m depth. These two changes are partly caused by the classification into the different fabrics needed for the calculation of the opening angles (Part 1, Diez et al., 2014). Below 1800 m depth the zero-offset velocity starts to increase with the stronger orientation of the c-axes towards the vertical. Corresponding to the change in the COF eigenvalues at 2040 m depth they reach a velocity of around 4010 m s^{-1}. We use this zero-offset P-wave velocity v_{p0} profile, from now on called EDML interval velocities, for later comparison with the velocity profile derived from the VSP measurement.

TCD
8, 4397–4430, 2014

4 Vertical seismic profiling (VSP)

A VSP survey has the advantage that the wave velocities can be calculated directly from the traveltimes due to the known travelpath in contrast to reflection seismic profiles where the depth of the layer is often unknown. By comparing velocities determined from the VSP survey and the COF eigenvalues we want to find out if absolute values and variations of either method match. This provides a general evaluation of the approaches and of the traveltime–depth conversion for locations of englacial seismic reflector depths.

The VSP data show clear signals from the direct wave (Fig. 4) travelling from the shot at the surface to the geophone within the borehole (Fig. 3). The detonation cord survey (survey 20120545, Fig. 4a) has a well defined onset of the first break. Some more variations can be observed in the booster data (survey 20120546, Fig. 4b). Strong noise is visible in most of the booster shots for traveltimes ≤ 0.2 s. For shot 11 the trigger did obviously not work correctly and in case of shot 14 strong noise throughout the record is visible, making it difficult to pick the signal of the direct wave.

We evaluate the variability of repeated explosive shots with the same charge size at the same location with the simultaneously recorded data from the 3C-geophones. For the detonation cord survey the first 9 shots are very similar, afterwards the shape of the wavelets become significantly more variable and the arrival times have variations of up to 1 ms. In case of the boosters as source variations are altogether larger with differences in the arrival time of up to 2 ms. Repeated shooting at the same point produced a hole of ~ 1 m depth over time. This might have changed the characteristics of the first break of the wavelet causing the variations in arrival time.

We picked the traveltime of every shot of the VSP survey with detonation cord and boosters to determine seismic velocity variations with depth. The data were resampled from 0.25 ms recording interval to 0.125 ms for a more precise picking of the first arrivals. Resampling was done with the seismic processing package ECHOS by a four-point interpolation filter. Some of the picks were corrected due to distinct changes in

TCD
8, 4397–4430, 2014

the traveltime observed in the data of the 3C-geophones like, for example, visible for shot 44 of the detonation cord survey. To reduce the picking error, the first break (fb), the first maximum (max) and the first zero crossing (zc) of the direct arrival were picked. This was done by two different persons to obtain statistical picking uncertainty.

From the picked traveltimes the interval velocities were calculated for the 40 m depth intervals between shots separately for the detonation cord and booster survey as well as for the different picks. Due to the shooting geometry (Fig. 3) the difference in travelpath from one shot to the next with the geophone at different depths is equal or smaller than the vertical geophone distance of 40 m. For the calculation of the interval velocities the difference in the travelpaths were used rather than the difference in borehole geophone depth. Further corrections were applied due to the elongation of the rope, which has an effect on the mean velocity. However, this effect is basically negligible for the interval velocities.

To jointly analyse the interval velocities derived from different picks of the wavelet (fb, max, zc) is only valid if the wavelet does not significantly change over depth due to, e.g. dispersion or frequency-dependent damping. For an unchanged wavelet shape over depth the traveltime difference between the picked maximum and the first break [max – fb], as well as the zero crossing and the first break [zc – fb] should be constant. However, the traveltime differences, i.e. the frequencies of the wavelet we observe are not constant over depth, hence, not independent of dispersion or frequency-dependent damping. While we observe an increase in frequency with increasing depth for the wavelets from the detonation cord survey, we observe a decrease in frequency over depth for the wavelets from the booster sources. We suggest that this signal trend is an effect of the repeated shooting at the same location rather than an indication of physical properties, like frequency-dependent damping.

Finally, to be able to compare the VSP velocities with the velocities calculated from the COF eigenvalues (Fig. 2c) a temperature correction has to be applied. The elasticity tensors of Gammon et al. (1983) was measured at −16 °C. Hence, we correct the VSP velocities with the gradient for P-waves given by Gammon et al. (1983) of

TCD
8, 4397–4430, 2014

$-2.3\,\mathrm{m\,s^{-1}\,K^{-1}}$ for the temperatures measured within the EDML borehole (Sect. 2.1). Thus, we obtain the interval velocities from the VSP measurements (Fig. 5, grey line) as a mean of all derived interval velocities of the different sources (booster, detonation cord) and picks from different wavelet regions (fb, max, zc, each from two different persons).

4.1 Comparison VSP and EDML interval velocities

The variations in the VSP interval velocities are rather large, with extrema up to $3350\,\mathrm{m\,s^{-1}}$ and $4800\,\mathrm{m\,s^{-1}}$. For improved clarity of the main velocity trend we apply a 200 m moving average to the VSP interval velocities (Fig. 5, black line). The grey area (Fig. 5) shows the root-mean-square (RMS) error calculated as the variations of the picked values to the moving average. The RMS errors of the VSP interval velocities are rather large, especially in the region between 1600 m depth and 2200 m depth. The large error in this region is attributed to incoherent excitation of elastic waves from the booster survey for shots 10 to 25 (Fig. 4b).

The vertical EDML and VSP interval velocities show good agreement above 1800 m depth with a velocity around $3870\,\mathrm{m\,s^{-1}}$. This is the region of cone fabric with large opening angles ($\leq$ 450 m depth) and girdle structures below (Fig. 2b). The VSP interval velocities show an increase to larger velocities ($\geq 4020\,\mathrm{m\,s^{-1}}$) at 1800 m depth. Some jumps in the calculated EDML interval velocities can be observed in this region. For the strongly developed cone fabric with small opening angles below 2030 m depth the VSP and EDML interval velocities agree well again with an average velocity of $\sim 4040\,\mathrm{m\,s^{-1}}$ for the VSP velocities and $\sim 30\,\mathrm{m\,s^{-1}}$ slower for the EDML velocities.

4.2 Different elasticity tensors

To evaluate the effect of different elasticity tensor on calculated P-wave velocities from COF data, the VSP interval velocities determined from first break, maximum and the zero crossing are considered separately in the following comparison (black lines,

TCD
8, 4397–4430, 2014

Fig. 6). We, thus, avoid including the effect of dispersion. The different elasticity tensors, calculated and measured, are given in Table 1.

The velocity profiles of the different picks (fb, max, zc) show slight variations, but the main trend is the same in all interval velocity profiles. For the first ~800 m higher velocities can be found for the interval velocities derived from the max and zc picks than for the fb picks. The VSP interval velocities are corrected for the temperature distribution within the ice sheet to −16 °C. Additionally, the velocities calculated using the elasticity tensor of Bennett (1988), given at −10 °C, are corrected to −16 °C as well.

The different vertical P-wave velocities calculated from the different elasticity tensors all follow the same velocity trend over depth, which is determined by the COF eigenvalues. The highest P-wave velocities are calculated from the theoretically derived elasticity tensor of Penny (1948), the lowest derived P-wave velocities from the elasticity tensor of Bass et al. (1957), who used the resonance frequencies to derive the components of the elasticity tensor. The velocities derived from the elasticity tensors of Gammon et al. (1983), Jona and Scherrer (1952) and Bennett (1988) all show good agreement with the VSP velocities.

This result is confirmed by the RMS differences that we calculate between the VSP interval velocities from first break, maximum and zero crossing picks and the EDML interval velocities derived with the different elasticity tensors (Table 1). Keeping the error bars in mind (up to ±350 m s^{-1}; Fig. 5, grey area) the velocities derived from the latter three elasticity tensors are all capable of explaining the velocity profile derived from the VSP survey by using the COF eigenvalues. The best accordance is gained using the elasticity tensor of Jona and Scherrer (1952). Neither of the elasticity tensors reaches the complete range of minimum and maximum interval velocities (3870–4040 m s^{-1}) of the VSP results. While the velocities derived by the Jona and Scherrer (1952) and Gammon et al. (1983) elasticity tensor fit well to the VSP velocities above 1800 m, hence, for lower velocities of ~3870 m s^{-1}, the ones derived from the Bennett (1988) elasticity tensor fit better below for the higher velocities of ~4040 m s^{-1} (Fig. 6). The larger depth interval between 200 m and 1800 m depth compared to the interval be-

TCD
8, 4397–4430, 2014

tween 1800 m and 2600 m depth is the reason why the RMS differences for the Gammon et al. (1983) and Jona and Scherrer (1952) elasticity tensor are slightly smaller than those for the Bennett (1988) elasticity tensor.

4.3 Discussion of VSP survey

The comparison of the interval velocities from the VSP survey and those derived from the COF eigenvalues show good agreement. The main trend of the VSP velocity profile, velocities $\sim 3870\,\mathrm{m\,s^{-1}}$ above 1800 m depth, an increase in velocity between 1800–2030 m depth and velocities $\sim 4040\,\mathrm{m\,s^{-1}}$ below 2030 m, can be reproduced with the calculations of velocities from the COF eigenvalue data.

The interval velocities derived from the VSP survey are compared to the zero-offset velocities calculated from the eigenvalues. As the shots during the survey were carried out on the surface 30 m away from the drill location of the EDML ice core (Fig. 3) the travelpath of the seismic wave is not zero-offset. The first measurement was done at a depth of 100 m. This corresponds to an angle between borehole and travelpath of 14.8°, neglecting effects of refraction within the firn. In the anisotropic case the velocity for an incoming angle θ of 14.8° differs of course from the zero-offset velocity we use for the comparison. For the existing anisotropy in this depth region, with a cone opening angle $\varphi = \chi \approx 75°$, the difference between the zero-offset velocity and the $v_p(\theta = 14.8°)$ is $< 5\,\mathrm{m\,s^{-1}}$. At the depth of 450 m where a stronger girdle anisotropy develops the angle between borehole and wave propagation θ is already only 3.7°. Thus, the error that is introduced by using the zero-offset EDML interval velocities for the comparison to the VSP interval velocities instead of the velocities corresponding to the actual angle between borehole and travelpath during the VSP survey is found to be negligible.

The small-scale variations in the EDML interval velocities reflect the increments of the COF eigenvalues and the classification of these eigenvalues in the different fabrics for the calculation of opening angles. This is especially obvious for the increase in velocity in the region between 1800 m and 2030 m depth, where the narrow cone fabric

TCD
8, 4397–4430, 2014

develops from the girdle fabric. Here, eigenvalues are classified as cone and girdle fabric alternately (Part 1, Diez et al., 2014). However, such small-scale variations are averaged out for the frequencies around 100 Hz, as we observe in our VSP survey and are, therefore, not visible.

In a recent study Gusmeroli et al. (2012) carried out an ultrasonic sounding experiment within the deep borehole at Dome C, East Antarctica, exciting P and vertical shear (SV) waves with frequencies of 23 kHz. Comparing their picked velocities from the ultrasonic sounding with velocities calculated by averaging the velocity for a vertical single maximum fabric for different incoming angles, as introduced by Bentley (1972), they found best agreement using the elasticity tensor derived by Dantl (1968). This is in strong contrast with our results, where the velocities derived with the elasticity tensor from Dantl (1968) (Fig. 6, red line) show a poor fit to the VSP interval velocities (Table 1). Possible reasons for this discrepancy include the methodological difference for velocity calculation or the fact that the samples in this VSP study are determined over significantly larger depth intervals from shot to shot than for the ultrasonic sounding. However, more likely is that the two orders of magnitude different frequencies are the cause. Unfortunately, we cannot discuss this issue further, as the frequency dependency of seismic wave velocities in ice is not yet fully determined.

5 Joint interpretation of seismic, radar and ice-core data

For a better understanding of the origin of laterally coherent englacial seismic and radar reflectors with a focus on changing COF we compare these data sets from Kohnen station (Fig. 1). As a reference we stack 60 traces of one seismic shot to increase the signal-to-noise ratio, without further processing. This allows us to identify distinct englacial reflections and directly compare seismic, radar and ice-core data characteristics in the depth domain in the following.

TCD
8, 4397–4430, 2014

5.1 Comparison of depth-dependent characteristics

Five regions are marked A–E in Fig. 7 which contain corresponding signals in at least two of the used data sets from ice core data (COF eigenvalues and grain radii), the stacked seismic trace and radar data, measured as well as modelled. We do not include a modelled seismic trace in this comparison. The problem is that modelling a seismic trace from the COF eigenvalues with a resolution of 50 m causes reflections at the depth where COF eigenvalues have been measured. This is not necessarily at the position of a COF transition, which is likely inadequately resolved. The modelled radar trace was calculated based on high-resolution conductivity measurements. However, the COF information has neither been taken into account here, for the above reason.

The radar reflection in region D was already connected to a change in COF (Fig. 7a) from girdle to cone fabric between 2025–2045 m depth by Eisen et al. (2007). Here, a strong signal can be seen in the 600 ns pulse radar trace (Fig. 7c, blue) as well as in the 60 ns pulse trace (Fig. 7c, red). Additionally, no corresponding signal can be found in the modelled radar trace (Fig. 7e). The periodic pattern of the traces with different air plane headings (Fig. 7d) indicates an orientation of girdle above cone fabric vertical and parallel to the ice divide (Eisen et al., 2007). This COF-induced radar reflection corresponds to a rather quiet zone within the seismic trace (Fig. 7b), followed by a distinct peak.

Further distinct signals marked A and B in the seismic trace correspond to clear signals in the radar data. The strongest seismic reflector is signal B. For both events strong reflections are visible within the 600 ns radar pulse (Fig. 7a, blue) and a clear signal in the 60 ns radar pulse (Fig. 7a, red). Additionally, no prominent signal can be observed in the modelled radar trace based on DEP measurements (Fig. 7e). Whether the radar signal differs for different air plane headings (Fig. 7d) is difficult to judge for event A due to strong noise. In case of event B the reflection is also clearly visible on the radar traces for the different air plane headings (Fig. 7d). Clear signals can be observed for headings in E, SE, W and NW directions and weaker reflections for the

TCD
8, 4397–4430, 2014

remaining directions. There seems to be a pattern in this reflection behaviour but not as clear as the pattern of event D. A jump in the COF eigenvalues (Fig. 7a) λ_2 and λ_3 can be observed over a very short depth interval at event B. In contrast, no variation in the COF eigenvalues can be observed in the region of event A. The grain radius data show a gradual change towards smaller grains at event A and towards larger grains at event B.

Event C shows a clear signal in the seismic trace, in strength similar to that of event D. The grain size for both event C and D shows a variation of the grain radius of ∼ 0.4–0.7 mm. However, at event C no clear signal can be observed in the radar data. In contrast, this is an extremely quiet zone within the trace of the 600 ns pulse (Fig. 7c, blue).

The deepest marked reflection is event E at a depth of ∼ 2350 m corresponding to a 50 m thick layer of girdle fabric within a region of strong developed cone fabric visible in the COF eigenvalues (Fig. 7a). A distinct change towards smaller grain radii can be observed in this region. A very small increase in reflection power near the noise floor seems to be observable on the 600 ns pulse (Fig. 7c, blue). However, no clear radar events are discernible in this depth range. In the seismic data a quiet zone is followed by a signal at the depth of ∼ 2350 m, the transition of the girdle fabric back to cone fabric.

5.2 Interpretation of englacial reflections

We interpret the reflectors in the radar data at 1690 m (event A) and 1810 m depth (event B) as being induced by changing COF, although no clear signals are observable in the COF eigenvalues. However, clear signals can be observed within the seismic and radar trace for both events. The COF eigenvalues in this region were measured with a resolution of ∼ 50 m. This resolution is not fine enough to show distinct changes over sub-wavelengths scales (several meters to tens of meters) that can cause reflections in the seismic and radar data. As expected, both events show no corresponding signal in the modelled radar trace.

TCD
8, 4397–4430, 2014

To estimate the strength of the reflectors from changing physical properties across the interface boundaries caused by the measured COF values we calculate the theoretical reflection coefficient for normal incidence, $R(0)$. We assume two semi-infinite half-spaces with the derived zero-offset velocities and use the Zoeppritz equation for the calculation of the reflection coefficient (e.g. Aki and Richards, 2002). The change in the COF eigenvalues corresponds to reflection coefficient of $R(0)|_B = 0.009$ for event B, $R(0)|_C = -0.006$ for event C and $R(0)|_D = 0.014$ for event D. These reflection coefficients for both interfaces are two orders of magnitude smaller than those of the ice–bed transition (Part 1, Diez et al., 2014).

The seismic reflection amplitude (Fig. 7b) of event C is significantly weaker than that of event B. Despite the difference of some 30 % in the calculated reflection coefficients this seems not adequate to explain the observed difference in the reflection amplitude. Even if geometrical spreading and damping are taken into account for event C, which is ∼150 m deeper than B, the observed difference in reflection amplitude cannot be fully accounted for. Reasons might be that the true change in anisotropy for event B is larger than resolved with the coarse eigenvalue measurements or that destructive interference occurs for event C.

In the seismic trace of event D a quiet zone is followed by a reflection about the same strength as that of event C, also the calculated reflection coefficient is twice as large. Concurrently, the COF eigenvalues change over a depth interval of 20 m. With maximum frequencies around 200 Hz the seismic data has a maximal resolution of ∼10 m. Thus, the transition from girdle to cone fabric over 20 m depth might be too gradual to cause a corresponding reflection. Another possibility might be that the observed change in eigenvalues is not an isolated transition, but several of these occur, causing partly destructive interference of the seismic wave. This could also explain the quiet zone above of the reflection at this depth. The strength of the reflection signal is further influenced by seismic trace stacking. Although this enhances the signal-to-noise ratio in general, it might also weaken some reflections, especially those from dipping reflectors as observed in the radar section (Fig. 8).

TCD
8, 4397–4430, 2014

A similar effect can be observed at event E. The 50 m thick layer of developed girdle fabric is visible in the COF eigenvalue data. This corresponds to a quiet zone followed by a clear reflection in the seismic data. The depth of this reflection fits to the transition back from girdle to cone fabric. In contrast, no clear signal can be observed for the transition from cone to girdle fabric 20 m above. This could be explained by a more gradual change from cone to girdle fabric while the transition from girdle to cone fabric occurs over a relatively sharp boundary. A second explanation is again the potential destructive interference of signals from the upper and lower transitions.

For event E, in addition to the variation in the COF eigenvalues a strong change can be observed in the grain radius. This raises the question if grain size determines the seismic reflectivity causally, too, or if this is merely a coincidence. In comparison, the changes in the grain radii are not large for the events A to D. Especially in case of events A and B, clear seismic and radar reflectors are observable, while the variations in grain radius are not significant. The observed variation in the VSP velocities (Sect. 4) argues as well against a dependency of seismic wave propagation primarily on grain size. The grain size increases continuously to about 2350 m depth where it decreases significantly (Fig. 7a, grey curve). If changes in the seismic velocity would directly depend on grain size, we would expect a decrease in seismic velocities below 2350 m to values like observed in the upper part of the ice sheet (above 500 m depth) where grain size is comparable. This is not the case (Fig. 5). Hence, we argue that the main cause for variations of seismic wave propagation are variations in the crystal orientation. However, we do not exclude the possibility that sudden changes in COF and grain size might be causally linked to the same underlying ice properties, such as impurity content.

5.3 Lateral coherency of COF-induced reflections

Our above investigation identified several reflections in seismic and radar data caused by changes in COF. This brings us in the position to evaluate the lateral coherency of these radar horizons in comparison to those caused by changes in conductivity. Fig-

TCD
8, 4397–4430, 2014

ure 8 shows extended parts of the radar surveys 023150 (60 ns pulse; b and d) and 022150 (600 ns pulse; c and e) with straight flight direction. Marked with light blue triangles and a light blue line are the two COF reflectors of Fig. 7, event B (~ 1800 m) and event D (~ 2035 m). The yellow triangles and yellow line mark the conductivity-induced reflection (Eisen et al., 2006), most likely caused by the 71 ± 5 kyr Toba volcanic eruption (Svensson et al., 2013).

In the single radar trace 4205 (Fig. 8a, red), closest to the EDML drill site, the conductivity-induced reflection is the strongest signal below 1700 m depth in the 60 ns pulse data, i.e. the data with higher vertical resolution. In contrast, the two COF-induced reflections are stronger than the conductivity-induced reflection in the 600 ns pulse data (Fig. 8a, blue). However, it is easier to trace the lateral extent of the COF-induced reflections in the 60 ns pulse data (Fig. 8b and d) than in the 600 ns pulse data.

Following the COF reflections in the wiggle plot of the 600 ns pulse (Fig. 8e) it becomes obvious that its characteristics are not as coherent in space as that of the conductivity-induced reflection. In both the 600 ns and 60 ns pulse data the strongest, most coherent reflector with laterally persistent attributes is the conductivity-induced event.

Based on these observations we conclude that the changes in COF are laterally much more variable than changes in conductivity. This makes intuitively sense, as changes in COF are developed in response to the local stress field within the ice, partly constrained by impurities, whereas changes in conductivity are formed by basically homogeneous deposition on the km-scale at the surface, with only slight post-depositional modification.

This finding is important for revisiting the physical properties of the echo-free zone (EFZ), which appears below ~ 2200 m depth, where no clear events are observable in the radar data. Drews et al. (2009) discussed reasons for the EFZ at Kohnen station and concluded that the EFZ is caused by layer roughness observed in line-scan data from the EDML ice core. Recent multi-static, phase-sensitive radar data show such rough basal layers above bedrock at many places in Antarctica (e.g. Gogineni,

TCD
8, 4397–4430, 2014

personal communication, 2014, Dahl-Jensen et al., 2014; Ross and Siegert, 2014) as well as Greenland (e.g. NEEM community members, 2013). Thus, it is evident that the occurrence of the EFZ depends on the technical capabilities of the radar systems, especially lateral resolution and sensitivity.

In contrast to the radar data, a clear signal can be seen within the EFZ region in the seismic data at 2400 m depth (Fig. 7, event E). The different characteristics in radar and seismic data at this depth can be attributed to the different horizontal and vertical resolution of either method, i.e. the difference in the size of the first Fresnel zone and vertical resolution. The first Fresnel zone for the seismic wave at this depth, with a mean frequency of ∼ 140 Hz, has a radius of about 180 m. The first Fresnel zone for the radar wave, with a frequency of 150 MHz, is about 35 m, i.e. the radar wave has a fivefold higher resolution than the seismic wave. However, at the same time the reflected radar signal is influenced by the smaller scale roughness, as indicated by Drews et al. (2009), and the effective radar signal is weakened within the EFZ. Hence, we can put forward the conclusion that the upper limit of the roughness scale of the physical properties causing the EFZ in traditional radar systems is smaller than the lateral resolution of the seismic data.

6 Conclusions

Our analyses of the EDML ice core and seismic data in the vicinity of the borehole at Kohnen station demonstrate that interval velocities determined from COF eigenvalues and VSP data are consistent within the available resolution and uncertainties. The choice of the monocrystal elasticity tensor for converting COF data to seismic velocities, however, has a strong influence on the results. Combining our findings with the result of Gusmeroli et al. (2012) raises the question on the frequency dependency of seismic wave velocities in ice. The components of the measured elasticity tensor should not only be considered to significantly depend on temperature (Gammon et al., 1983), but also on frequency. Further, based on the derived reliable depth conversion

TCD
8, 4397–4430, 2014

for the seismic data and the comparison to ice core data, we conclude that observed englacial reflections in the seismic data are caused by short-scale changes in COF and not by variations in grain size.

By comparing seismic, radar and ice-core data to determine the origin or radar reflections, we find that lateral characteristics of COF-induced radar reflections are subject to much more lateral variations than conductivity-induced reflections. Nevertheless, as the resolution of available COF data is not fine enough compared to the wavelengths of geophysical methods, there is still a need for very high resolution measurement with fabric analysers or ultrasonic logging on ice cores or in boreholes to fully understand the formation and distribution of crystal fabric and its interaction with impurities in the ice.

Without ice cores or seismic data at hand, it remains a challenge to single out COF-induced reflectors within the larger number of conductivity-induced reflections in radar data sets. Our approach shows how a combination with seismic data can considerably reduce ambiguities. We therefore recommend to carry out dedicated local seismic surveys during pre-site surveys of upcoming ice-core deep drilling projects, such as to retrieve Antarctica's oldest ice (Fischer et al., 2013). COF-based reflectors can be identified in combined data sets and only those radar reflectors be used for extrapolating already established age–depth scales from other ice cores, which are purely caused by changes in conductivity and, thus, true isochrones.

Our analysis of radar and seismic data within the radar EFZ allowed us to limit the previously unknown lateral roughness of physical properties to a scale smaller than the typical horizontal resolution on the order of 100 m (size of the first Fresnel zone) of the seismic data. While this could rather represent the specific ice-dynamic setting at the EDML drill site than a universally valid value, the progress in radar imaging in the recent years and the widespread observation of a basal layer in Antarctica and Greenland confirm roughness scales of basal layers on the order of hundred meters. While it has already been shown that the paleo-climate proxy records in such basal

TCD
8, 4397–4430, 2014

layers are most likely disturbed (e.g. NEEM community members, 2013), their role for ice viscosity and, thus, ice dynamics and flow still requires further investigations.

Acknowledgements. We are grateful for the invaluable support of the AWI logistic team at Kohnen station, especially Cord Drücker, Holger Wohltmann and Jens Köhler. We thank Rick Blenkner, Pascal Bohleber and Sverrir Hilmarsson for their support during the campaigns, as well as Thomas Bohlen and his group of the Karlsruhe Institute of Technology for their support during this study. We thank CIC, University of Copenhagen for the provision of the temperature logger. Financial support for this study was provided to O.E. by the German Science Foundation (DFG) "Emmy Noether"-program grant EI 672/5-1. I.W. was supported by the Initiative and Networking Fund of the Helmholtz Association (HGF–VH-NG-802) and T.B. by the German Science Foundation (DFG) through the grant GA1271/8-1 within the Priority Program SPP-1158.

References

Aki, K. and Richards, P. G.: Quantitative Seismology, University Science Books Sausalito, California, 2002. 4413

Bass, R., Rossberg, D., and Ziegler, G.: Die elastischen konstanten des Eises, Z. Phys., 149, 199–203, 1957. 4408, 4422

Bennett, H. F.: An investigation into velocity anisotropy through measurements of ultrasonic wave velocities in snow and ice cores from Greenland and Antarctica, Ph. D. thesis, University of Wisconsin-Madison, Ann Arbor, MI, UMI, 1988. 4408, 4409, 4422

Bentley, C. R.: Seismic-wave velocities in anisotropic ice: a comparison of measured and calculated values in and around the deep drill hole at Byrd Station, Antarctica, J. Geophys. Res., 77, 4406–4420, 1972. 4410

Binder, T.: Measurements of grain boundary networks in deep polar ice cores – a digital image processing approach, Ph. D. thesis, Ruperto-Carola University Heidelberg, Germany, 2014. 4400

Brockamp, B. and Querfurth, H.: Untersuchungen über die Elastizitätskonstanten von See- und Kunsteis, Polarfoschung, 34, 253–262, 1964. 4422

Cuffey, K. M. and Paterson, W. S. B.: The Physics of Glaciers, Elsevier, 2010. 4398

TCD
8, 4397–4430, 2014

Dahl-Jensen, D., Gogineni, S., and Panton, C.: Disturbed basal ice seen in radio echo images coincide with zones of big interlocking ice crystals, Geophys. Res. Abstr., 16, EGU2014-9677, 2014. 4416

Daley, P. F. and Krebes, E. S.: Alternative linearized exoressions for qP, qS1 and qS2 phase velocities in a weakly anisotropic orthorombic medium, CREWES Res. Rep., 16, 1–19, 2004. 4403

Dantl, G.: Die elastischen Moduln von Eis-Einkristallen, Phys. kondens. Mater., 7, 390–397, 1968. 4410, 4422

Diez, A. and Eisen, O.: Seismic wave propagation in anisotropic ice – Part 1: Elasticity tensor and derived quantities from ice-core properties The Cryosphere Discuss., 8, 4349–4395, doi:10.5194/tcd-8-4349-2014, 2014. 4399, 4403, 4404, 4410, 4413

Drews, R., Eisen, O., Weikusat, I., Kipfstuhl, S., Lambrecht, A., Steinhage, D., Wilhelms, F., and Miller, H.: Layer disturbances and the radio-echo free zone in ice sheets, The Cryosphere, 3, 195–203, doi:10.5194/tc-3-195-2009, 2009. 4415, 4416

Drews, R., Martin, C., Steinhage, D., and Eisen, O.: Characterizing the glaciological conditions at Halvfarryggen ice dome, Dronning Maud Land, Antarctica, J. Glaciol., 59, 9–20, 2013. 4401

Eisen, O., Wilhelms, F., Steinhage, D., and Schwander, J.: Instruments and methods: improved methode to determine radio-echo sonding reflector depth from ice-core profiles of permittivity and conductivity, J. Glaciol., 52, 299–310, 2006. 4400, 4415

Eisen, O., Hamann, I., Kipfstuhl, S., Steinhage, D., and Wilhelms, F.: Direct evidence for continuous radar reflector originating from changes in crystal-orientation fabric, The Cryosphere, 1, 1–10, doi:10.5194/tc-1-1-2007, 2007. 4400, 4401, 4411, 4429

Eisen, O., Hofstede, C., Diez, A., Kristoffersen, Y., Lambrecht, A., Mayer, C., Blenkner, R., and Hilmarsson, S.: Operational vibroseis systems for long-distance on-ice seismic surveys, Polar Sci., under review., 2014. 4401

Fischer, H., Severinghaus, J., Brook, E., Wolff, E., Albert, M., Alemany, O., Arthern, R., Bentley, C., Blankenship, D., Chappellaz, J., Creyts, T., Dahl-Jensen, D., Dinn, M., Frezzotti, M., Fujita, S., Gallee, H., Hindmarsh, R., Hudspeth, D., Jugie, G., Kawamura, K., Lipenkov, V., Miller, H., Mulvaney, R., Parrenin, F., Pattyn, F., Ritz, C., Schwander, J., Steinhage, D., van Ommen, T., and Wilhelms, F.: Where to find 1.5 million yr old ice for the IPICS "Oldest-Ice" ice core, Clim. Past, 9, 2489–2505, doi:10.5194/cp-9-2489-2013, 2013. 4417

TCD
8, 4397–4430, 2014

Fujita, S., Matsuoka, T., Ishida, T., Matsuoka, K., and Mae, S.: A summary of the complex dielectric permittivity of ice in the megahertz range and its application for radar sounding of polar ice sheets, in: The Physics of Ice Core Records, edited by: Hondoh, T., Hokkaido-University Press, 185–212, Shikotsukohan, Hokkaido, Japan, 14–17 September 1998, http://hdl.handle.net/2115/32469, 2000. 4399

Gammon, P. H., Kiefte, H., Clouter, M. J., and Denner, W. W.: Elastic constant of artificial and natural ice samples by brillouin spectroscopy, J. Glaciol., 29, 433–460, 1983. 4399, 4404, 4406, 4408, 4409, 4416, 4422

Green, R. E. and Mackinnen, L.: Determination of the Elastic Contants of ice single crystals by ultrasonic pulse method, J. Acoust. Soc. Am., 28, 1292, 28, p. 1292, 1956. 4422

Gusmeroli, A., Pettit, E. C., Kennedy, J. H., and Ritz, C.: The crystal fabric of ice from full-waveform borehole sonic logging, J. Geophys. Res., 117, F03021, doi:10.1029/2012JF002343, 2012. 4410, 4416

Hamann, I., Kipfstuhl, S., and Lambrecht, A.: Fabrics and grain-shape orientations in EDML ice core, Antarctica, in: The 28th NIPR Symposium on Polar Meteorology and Glaciology, 30. November–1. Dezember 2005, National Institute of Polar Research, Tokyo, Japan, 2005. 4400

Jona, F. and Scherrer, P.: Die elastischen Konstanten von Eis-Einkristallen, Helv. Phys. Acta, 25, 35–54, 1952. 4408, 4409, 4422

Matsuoka, T., Fujita, S., Morishima, S., and Mae, S.: Precise measurement of dielectric anisotropy in ice Ih at 39 GHz, J. Appl. Phys., 81, 2344–2348, 1997. 4399

NEEM community members: Eemian interglacial reconstructed from a Greenland folded ice core, Nature, 493, 489–494, 2013. 4416, 4418

Oerter, H., Drücker, C., Kipfstuhl, S., and Wilhelms, F.: Kohnen station – the drilling camp for the EPICA deep ice core in Dronning Maud Land, Polarforschung, 78, 1–23, 2009. 4400

Penny, A. H. A.: A theoretical determination of the elastic constants of ice, Math. Proc. Cambridge, 44, 423–439, 1948. 4408, 4422

Ross, N. and Siegert, M.: Concentrated englacial shear over rigid basal ice, West Antarctica: implications for modelling and ice sheet flow, Geophys. Res. Abstr., 16, EGU2014–5568, 2014. 4416

Svensson, A., Bigler, M., Blunier, T., Clausen, H. B., Dahl-Jensen, D., Fischer, H., Fujita, S., Goto-Azuma, K., Johnsen, S. J., Kawamura, K., Kipfstuhl, S., Kohno, M., Parrenin, F., Popp, T., Rasmussen, S. O., Schwander, J., Seierstad, I., Severi, M., Steffensen, J. P., Ud-

TCD
8, 4397–4430, 2014

isti, R., Uemura, R., Vallelonga, P., Vinther, B. M., Wegner, A., Wilhelms, F., and Winstrup, M.: Direct linking of Greenland and Antarctic ice cores at the Toba eruption (74 ka BP), Clim. Past, 9, 749–766, doi:10.5194/cp-9-749-2013, 2013. 4415

Weikusat, I., Kipfstuhl, S., Faria, S. H., Azuma, N., and Miyamoto, A.: Subgrain boundaries and related microstructural features in EDML (Antarctica) deep ice core, J. Glaciol., 55, 461–472, 2009. 4400

Wilhelms, F., Sheldon, S. G., Hamann, I., and Kipfstuhl, S.: Implications for and findings from deep ice core drillings an example: The ultimate tensil strength of ice at high strain rates, Physics and Chemistry of Ice, in: Proceedings of the International Conference on the Physics and Chemistry of Ice held at Bremerhaven, Germany on 23–28 July 2006, The Royal Society of Chemistry Special Publication No. 311, 635–639, 2007. 4400

TCD
8, 4397–4430, 2014

Table 1. Different elasticity tensors, measured and calculated (values in 10^9 N m^{-2}). The order follows later calculations of the P-wave velocities from lower to higher velocities using the given elasticity values. The second part of the table gives the RMS error in m s^{-1} calculated from the VSP interval velocities derived from first break (fb), maximum (max) and zero crossing (zc) picks in comparison to the EDML interval velocities derived from the COF eigenvalues.

	Elasticity tensor					RMS error		
	C_{11}	C_{33}	C_{55}	C_{12}	C_{13}	fb	max	zc
Bass et al. (1957)	13.3 ± 0.8	14.2 ± 0.7	3.06 ± 0.015	6.3 ± 0.8	4.6 ± 0.9	147	160	155
Green and Mackinnen (1956)	13.33 ± 1.98	14.28 ± 0.54	3.26 ± 0.08	6.03 ± 0.72	5.08 ± 0.72	115	125	121
Dantl (1968)	13.21 ± 0.04	14.43 ± 0.06	2.89 ± 0.02	6.7 ± 0.13	5.79 ± 0.41	106	117	112
Brockamp and Querfurth (1964)	13.63	14.85	3.04	6.69	(5.19)	79	87	83
Gammon et al. (1983)	13.93 ± 0.04	15.01 ± 0.05	3.01 ± 0.01	7.08 ± 0.04	5.77 ± 0.02	**59**	**61**	**57**
Jona and Scherrer (1952)	13.845 ± 0.08	14.99 ± 0.08	3.19 ± 0.03	7.07 ± 0.12	5.81 ± 0.16	**58**	**57**	**54**
Bennett (1988)	14.06 ± 0.08	15.24 ± 0.12	3.06 ± 0.03	7.15 ± 0.15	5.88 ± 0.25	**62**	**53**	**52**
Penny (1948)	15.2	16.2	3.2	8	7	171	155	159

TCD
8, 4397–4430, 2014

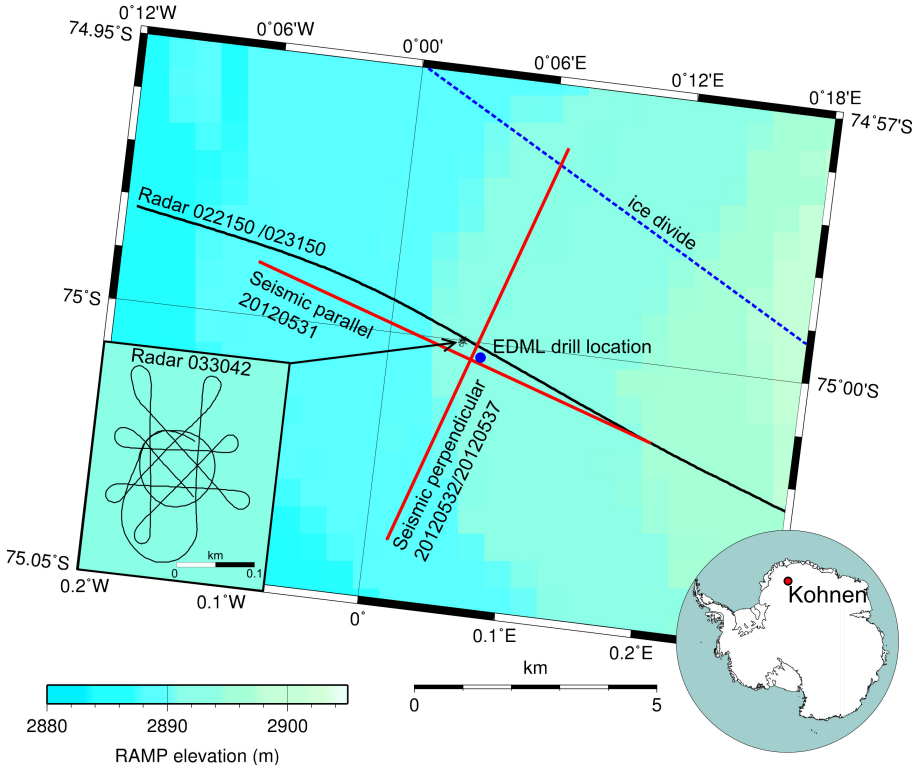

Figure 1. Different surveys carried out at Kohnen station, Dronning Maud Land, Antarctica (Inset of Antarctica "SCAR Antarctica Digital Database"). Geometry of seismic wideangle survey carried out in January 2012 and 2013, with explosives and vibroseis as source (red lines). Two lines were shot, one parallel (survey 20120531) and one perpendicular (20120532/20120537) to the ice divide. The blue dot marks the drill location of the EDML ice core. The flight line of the radar survey 022150 (600 ns pulse) and 023150 (60 ns pulse) is plotted in black. The inset shows the survey 033042 (60 ns pulse) done with the air plane driving on the ground.

TCD
8, 4397–4430, 2014

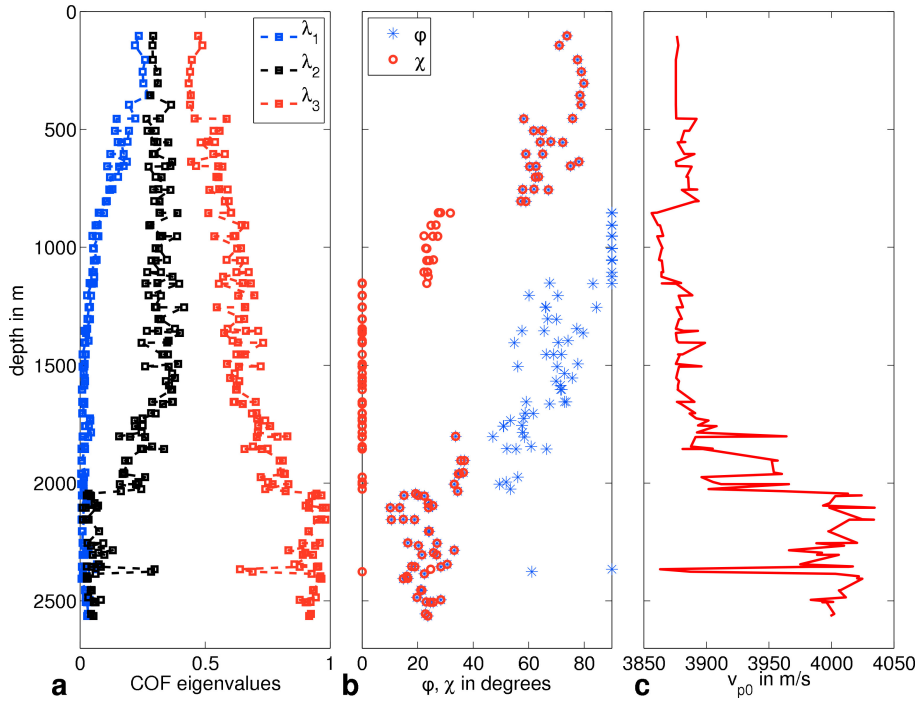

Figure 2. (a) COF eigenvalues derived from the orientation tensor measured on thin section of the ice core EDML. **(b)** Opening angles derived from the eigenvalues in **(a)**. Regions with $\varphi = \chi$ contain cone fabrics, regions with $\varphi = 90^\circ$ contain thick girdle fabrics and regions with $\chi = 0^\circ$ contain partial girdle fabric. **(c)** Zero-offset P-wave velocity v_{p0} calculated from the elasticity tensors derived from the opening angles in **(b)**.

TCD
8, 4397–4430, 2014

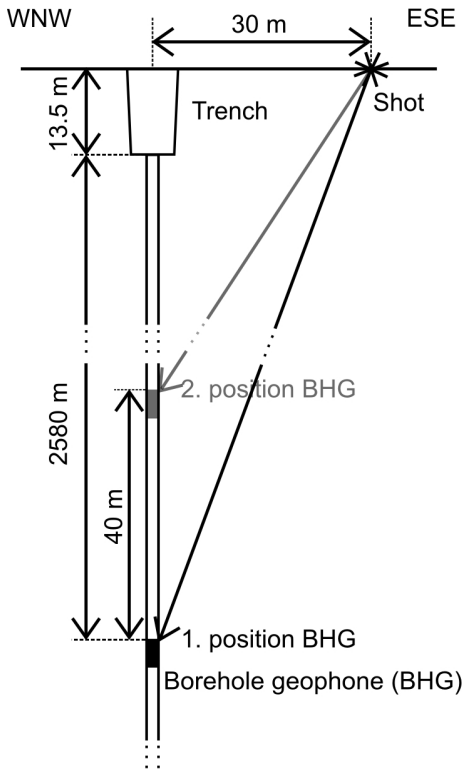

Figure 3. Geometry setup for shooting of VSP survey. The shot location was 30 m away from the borehole location. The borehole geophone (BHG) was pulled up in intervals of 40 m from a depth of 2580 m to 60 m depth for the detonation cord as source. The survey was complemented between 2560 m and 1600 m with boosters as source and locations of the borehole geophone shifted by 20 m to the previous survey. The depth is given to the top of the borehole casing, measured to be 13.5 m below the surface (January 2012).

TCD
8, 4397–4430, 2014

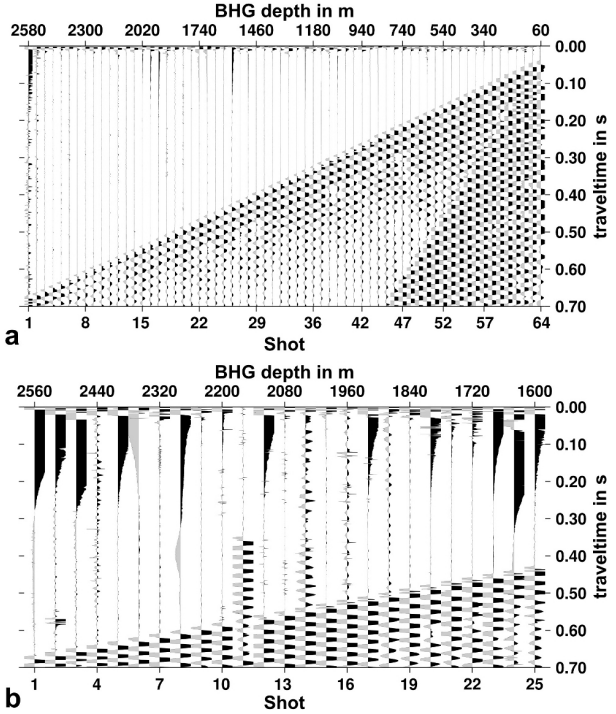

Figure 4. Recorded first arrivals from the VSP surveys with detonation cord (**a**, survey 20130545) and booster (**b**, survey 20130546) as source. The top ordinate gives the location, hence, the depth of the borehole geophone (BHG), the bottom ordinate shows the shot number. In **(a)** not only the direct P-wave arrival is visible but also a borehole guided wave travelling with a velocity of 1150 m s^{-1}. Depth is given here to top of casing.

TCD
8, 4397–4430, 2014

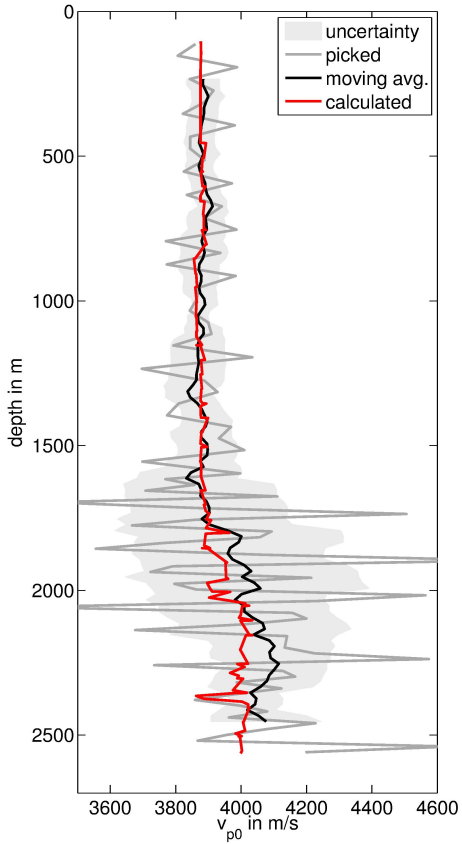

Figure 5. Average interval velocity (grey line) derived from the traveltimes of the detonation cord and booster survey for the three different picks (first break, maximum, zero crossing). The black line shows the moving average with a sliding window of 200 m and its RMS error (grey area). These interval velocities are temperature corrected to −16 °C. The red line shows the v_{p0} interval velocity calculated from the COF eigenvalues of the EDML ice core as given in Fig. 2.

TCD
8, 4397–4430, 2014

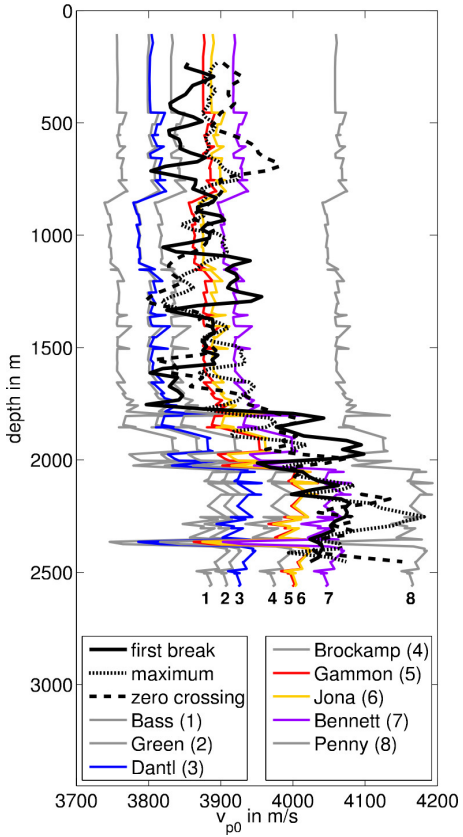

Figure 6. Comparison of vertical P-wave velocities calculated from the EDML eigenvalues with different elasticity tenors (Table 1) with the interval velocities derived from the VSP data sets for the first break, the maximum and the zero crossing (black lines).

TCD
8, 4397–4430, 2014

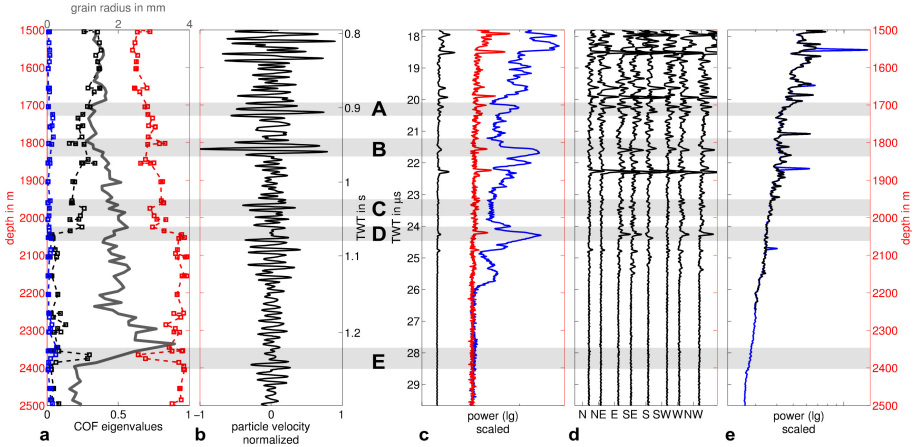

Figure 7. Comparison of ice-core COF eigenvalues and grain radius r (diameter $d = 2r$) **(a)**, with a stacked seismic trace of survey 20120537 **(b)**, radar data **(c, d)** and modelled (synthetic) radar data **(e)**. The seismic trace is a stack of 60 channels, unfiltered data of an explosive survey carried out in a 30 m deep borehole. The normal-moveout correction was done with the velocities derived from the VSP survey. **(c)** shows the radar traces closest to the EDML drill location from the survey 022150 (600 ns pulse) in blue and 023150 (60 ns pulse) in red, together with a stack of all traces of the survey 033042 (60 ns pulse) in black. **(d)** shows stacked traces of the survey 033042 for different air plane headings, i.e. different polarisations (Fig. 1). **(e)** is a forward modelled radar trace from DEP measurements with (blue) and without (black) conductivity peaks (Eisen et al., 2007). All figures are plotted over depth (red axis), with additionally marking the TWT on the seismic and radar traces (black axis). The calculation of depth from TWT was done with the VSP velocities in case of the seismic data and with a constant velocity of 168.7 m μs^{-1}, with a firn correction of 13 m in case of the radar data. The marked events A–E are discussed in the text.

TCD
8, 4397–4430, 2014

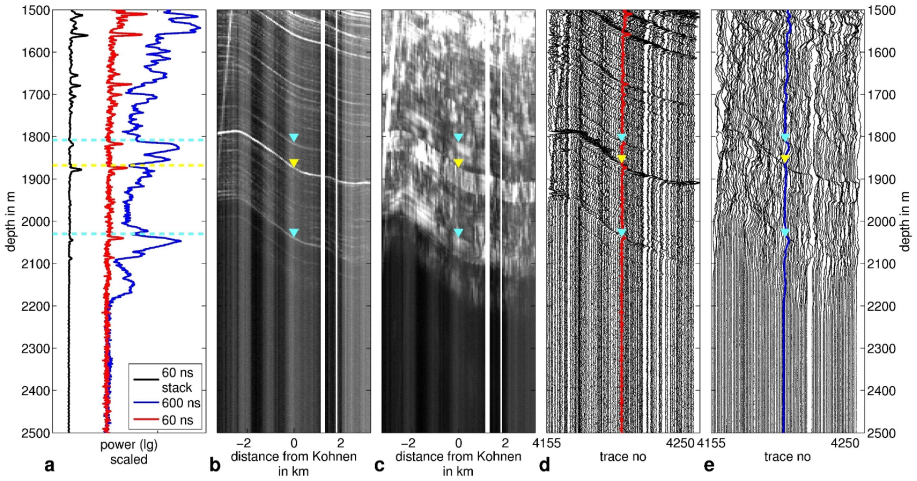

Figure 8. Radar data from Kohnen station with 60 ns pulse (023150) and 600 ns pulse (022150) as density plot (**b** and **c**, respectively) and wiggle plot (**d** and **e**, respectively). Subfigure **(a)** shows the trace closest to the EDML drill location of the 60 ns pulse (red) and 600 ns pulse (blue) survey, as well as the stack of all traces of survey 033042 (same figure as Fig. 7c). TWT-depth conversion as in Fig. 7. The light blue triangle and lines indicate COF-induced reflections whereas the yellow triangles and line show a conductivity-induced reflection for comparison.

TCD
8, 4397–4430, 2014